

UC Irvine

UC Irvine Previously Published Works

Title

Tunable optical response of bowtie nanoantenna arrays on thermoplastic substrates

Permalink

<https://escholarship.org/uc/item/62j1g3d6>

Journal

Nanotechnology, 27(10)

ISSN

0957-4484

Authors

Sharac, N
Sharma, H
Veysi, M
[et al.](#)

Publication Date

2016-03-11

DOI

10.1088/0957-4484/27/10/105302

Peer reviewed

PAPER

Tunable optical response of bowtie nanoantenna arrays on thermoplastic substrates

To cite this article: N Sharac *et al* 2016 *Nanotechnology* **27** 105302

View the [article online](#) for updates and enhancements.

Related content

- [Sensing using plasmonic nanostructures and nanoparticles](#)
Judith Langer, Sergey M Novikov and Luis M Liz-Marzán
- [Large-area, reproducible and sensitive plasmonic MIM substrates for surface-enhanced Raman scattering](#)
Kuanguo Li, Yong Wang, Kang Jiang *et al.*
- [Highly sensitive and scalable AAO-based nano-fibre SERS substrate for sensing application](#)
L K Lim, B K Ng, C Y Fu *et al.*

Recent citations

- [Mechanically tunable sub-10 nm metal gap by stretching PDMS substrate](#)
Wenjie Liu *et al*



IOP | ebooks™

Bringing you innovative digital publishing with leading voices to create your essential collection of books in STEM research.

Start exploring the collection - download the first chapter of every title for free.

Tunable optical response of bowtie nanoantenna arrays on thermoplastic substrates

N Sharac¹, H Sharma², M Veysi³, R N Sanderson⁴, M Khine^{2,5},
F Capolino³ and R Ragan²

¹Department of Chemistry, University of California, Irvine, Irvine, CA 92697-2025, USA

²Department of Chemical Engineering and Materials Science, University of California, Irvine, Irvine, CA 92697-2575, USA

³Department of Electrical Engineering and Computer Science, University of California, Irvine, Irvine, CA 92697-2625, USA

⁴Department of Physics and Astronomy, University of California, Irvine, Irvine, CA 92697-4575, USA

⁵Department of Biomedical Engineering, University of California, Irvine, Irvine, CA 92697-2700, USA

E-mail: rragan@uci.edu

Received 13 September 2015, revised 7 January 2016

Accepted for publication 13 January 2016


Published 11 February 2016



CrossMark

Abstract

Thermally responsive polymers present an interesting avenue for tuning the optical properties of nanomaterials on their surfaces by varying their periodicity and shape using facile processing methods. Gold bowtie nanoantenna arrays are fabricated using nanosphere lithography on prestressed polyolefin (PO), a thermoplastic polymer, and optical properties are investigated via a combination of spectroscopy and electromagnetic simulations to correlate shape evolution with optical response. Geometric features of bowtie nanoantennas evolve by annealing at temperatures between 105 °C and 135 °C by releasing the degree of prestress in PO. Due to the higher modulus of Au versus PO, compressive stress occurs on Au bowtie regions on PO, which leads to surface buckling at the two highest annealing temperatures; regions with a 5 nm gap between bowtie nanoantennas are observed and the average reduction is 75%. Reflectance spectroscopy and full-wave electromagnetic simulations both demonstrate the ability to tune the plasmon resonance wavelength with a window of approximately 90 nm in the range of annealing temperatures investigated. Surface-enhanced Raman scattering measurements demonstrate that maximum enhancement is observed as the excitation wavelength approaches the plasmon resonance of Au bowtie nanoantennas. Both the size and morphology tunability offered by PO allows for customizing optical response.

 Online supplementary data available from stacks.iop.org/NANO/27/105302/mmedia

Keywords: plasmonics, thermoplastic films, plasmon resonance, surface-enhanced Raman scattering

(Some figures may appear in colour only in the online journal)

1. Introduction

Nanoarchitectures with subwavelength building blocks lead to enhanced light–matter interactions due to the coupling between electromagnetic waves and collective charge density fluctuations; i.e., surface plasmons. Engineering hot spots,

regions with significantly enhanced electric fields due to coupling at the plasmon resonance in nanostructures, have been heavily pursued since the first measurement of enhanced Raman scattering intensity at roughened electrodes [1] and later through reports of single molecule detection in surface-enhanced Raman scattering (SERS) [2, 3]. Hotspots, resulting

from localized surface plasmon resonance (LSPR), have demonstrated utility in a variety of applications, from molecular detection in both SERS [4] and metal-enhanced fluorescence (MEF) [5, 6] to improving the performance of photovoltaics [7]. For example, the ability to tune the plasmon resonance, affected by geometrical parameters and substrate permittivity, is beneficial for engineering spectral overlap with the excitation wavelength of an appropriate fluorophore in MEF and to control interactions with biological samples [8]. Improving the photovoltaic efficiency also requires control of resonance wavelength, density and permittivity [9] in order to maximize light scattering, increase optical absorption in the active region, and minimize parasitic absorption of plasmonic nanostructures [10]. It is well known that the intensity and wavelength of LSPR can be tuned by changing the material (permittivity), size, shape, geometric arrangement of nanostructures, or the dielectric environment [11]. Some authors have previously shown, using in-house codes and finite element method simulations, that ordered arrays of nanoantennas or nanoclusters lead to sharp Fano resonances with enhanced electric [12, 13] or magnetic [14] fields when illuminated by plane waves. In particular, these resonances, whose frequencies vary with the angle of incidence, exhibit a narrower linewidth than the resonance of the isolated nanoantenna or nanocluster. This body of work motivates the need for fabrication methods to achieve periodic arrays of metal architectures with tunable LSPR. Top-down, planar lithographic approaches such as photolithography, electron beam lithography [15–17] and ion beam lithography [18] achieve a variety of nanoscale patterns but are typically expensive and often have a low throughput, which typically limits area coverage [19]. In contrast, self-assembly approaches such as nanosphere lithography (NSL) [20] and chemical assembly [21–26] offer the ability to create nanoscale feature advantages at a lower cost with higher throughput. The use of self-organized diblock copolymers, by annealing near glass transition temperature, has been shown to serve as a template for ordering nanostructures [21, 25, 26]; however, to achieve a complex pattern, diblock copolymers must be organized on lithographically prepared templates [27]. In addition, bowtie nanoantenna arrays of various sizes can be fabricated using NSL, although the gap spacing and bowtie area size are not independently tunable. Self-assembly alone can be limited in terms of the versatility of achievable patterns [19]. While past experiments have used elastomeric substrates to stretch metamaterial and plasmonic arrays, this tunability in size has been limited to enlarging features, rather than reducing them [28–30].

Here we present a facile method to form arrays of Au bowtie nanoantennas with the ability to tune feature size, gap spacing and interaction volume via surface buckling over large areas by utilizing NSL and annealing of prestressed, thermoplastic polyolefin (PO) films post-metal deposition. Upon heating the PO film above its glass transition temperature (95 °C), the PO film and features on the surface shrink [31]. Nguyen *et al* were first to report a 95% reduction in area and 77% reduction in length of laser printed channels to fabricate microfluidic channels on PO [32]. The achievable

size reduction of PO [32] exceeds that of polystyrene [23] and is beneficial to achieving smaller gap spacings in nanostructure arrays. The gap spacing is critical, as finite element simulations have shown that the electric field strength ($|\mathbf{E}|$) is highest in the gap of bowtie nanoantennas, for example, and increases with decreasing the gap size [33–35] when the gap spacing is below 50 nm [36–39]. For example, the enhanced electric field intensity ($|\mathbf{E}|^2$) in the gap region is reported to reach values larger than 10^3 when the gap size in a Au bowtie nanoantenna decreases to values less than 20 nm [36, 37]. Furthermore, since the LSPR frequency is related to the geometrical features of the bowtie antennas, we show both are tunable via the thermoplastic processing conditions described in this paper. In particular, processing the prestressed PO film at different degrees of temperature, post-metal deposition, systematically reduces the dimensions of triangles in the bowtie nanoantenna and gap spacings between the triangles. The reduction in PO areas with and without Au on the surface differs since Au has a stiffer modulus than PO. At the maximum processing temperature investigated, buckling of the surface is observable and this opens another avenue for tuning optical properties. Whitesides *et al* were the first to investigate buckling pattern formation by forming Au thin films and periodically varying the Young's modulus on elastomeric polydimethylsiloxane (PDMS) surfaces [40, 41]. Recently, experimental studies coupled with finite element analysis have examined buckling in the large deformation limit for nanoscale patterns [42–44]. The resulting buckled structures of nanopatterned surfaces differ significantly in amplitude and wavelength from the thin film, and the small deformation limit and the critical stress at which buckling occurs increases [44]. Gao *et al* also demonstrated that surface buckling will lead to a shift in the optical transmission window of metal nanorods on PDMS [44].

Here, optical properties of Au bowtie nanoantennas are investigated experimentally and theoretically in both the pre-buckling and buckling regime by systematically relieving the prestress with processing temperature. Reflectance spectroscopy measures a blue shift of the plasmon resonance wavelength with increasing processing temperature; a 90 nm window for tuning the LSPR wavelength is measured. Electromagnetic simulations elucidate that surface buckling plays a role in the measured LSPR shift. SERS measurements were performed at two excitation wavelengths, 633 nm and 785 nm; the maximum enhancement factor (EF), defined as the ratio of the SERS signal to the Raman signal, was observed as the excitation wavelength approached the LSPR wavelength, as determined from the maximum value in reflectance measurements. This tunability from NSL bowtie nanoantennas is a promising first demonstration, as NSL is able to generate versatile patterns when combined with reactive ion etching [45] and multilayer masks [46]. This tunable thermoplastic approach is also compatible with other lithographic approaches [47]. The work presented here is an important step in achieving complex architectures on the sub-lithographic length scale using inexpensive lithographic methods, and can be used to improve periodicity of any lithographic method. Both of these advantages are particularly important for experiments that

study plasmon coupling [48, 49], which depend on gaps changing by nanometer and even sub-nanometer differences, the latter exceeding the resolution attained by electron beam lithography. Overall, thermoplastic surfaces also provide an exciting avenue to generate non-planar plasmonic and meta-surfaces to further tune optical properties [40, 43, 44].

2. Methods

2.1. Bowtie fabrication

Au bowtie nanoantennas were fabricated on prestressed PO films (955-D, Sealed Air Corporation), a thermoplastic polymer. PO films, with a thickness of approximately 1 mm and laminated on 3-mm-thick polyester, were cleaned in isopropyl alcohol and dried with pressurized air. The PO film was then corona-treated for 35 s to increase the hydrophilicity of the surface. A 10.1 wt% solid suspension of 500 nm carboxylate polystyrene (PS-COOH) microspheres (Bangs lab) was diluted to a 3:1 ratio with Triton X-100 and methanol (1:400 by volume) to serve as a deposition mask [20]. Approximately 12 μl of this solution was then deposited onto the PO films using a spin coater for 5 min at a speed of 1200 RPM. Samples were then allowed to dry for two hours. Afterwards, the samples were etched in an oxygen plasma asher for 30 s at a power of 20 W. A 3 nm Cr adhesion layer and then a 40 nm Au layer were deposited on the samples using physical vapor deposition in a Temescal CV-8 electron beam evaporator. Temperatures did not exceed 100 °C during the deposition process to avoid premature shrinking of PO films. The samples were then sonicated in ethanol for 2 min followed by sonication in Millipore water to remove the PS-COOH microspheres in order to yield an array of Au bowties. To keep the PO surface from deforming, the sonication was performed in an ice bath. The samples were left to dry in ambient conditions overnight.

2.2. Prestress relief

The PO samples with polyester backing were mounted on a glass slide with double-sided tape and heated in a convection oven from room temperature to processing temperatures that ranged from 105 °C to 135 °C. Samples were annealed with a starting temperature of approximately 60 °C, and ramped up to temperatures at intervals of 5 °C–10 °C. Once reaching the designated processing temperature, the sample was held at this temperature until the prestress relief for this temperature was complete, as measured, macroscopically, by digital calipers. The time period for which the sample was held at the final temperature was between 10 and 30 min. The macroscopic size reduction was measured with digital calipers after heat treatment. The percentage size reduction was calculated by taking the ratio of the final length and width of PO samples relative to the polyester backing, as the polyester backing does not shrink during heat treatment. Samples that were not heat-treated were also analyzed for reference.

2.3. Characterization of morphology

Atomic force microscopy (AFM) was performed to characterize sample topography using an Asylum Research MFP 3D AFM (Santa Barbara, CA, USA) using AFM probes with 75 kHz resonance frequency and a diamond-like carbon coating (ACST-50, Budget Sensors). Scanning electron microscopy (SEM) was used to image bowtie feature size and periodicity using an FEI-Magellan 400 XHR at 3 kV as a function of heat treatment temperature. Bowtie gap spacing was measured and averaged over areas greater than 1 $\mu\text{m} \times 1 \mu\text{m}$ from SEM images, using ImageJ. The measured change in size reduction from SEM data was compared to the macroscopic size reduction obtained using digital calipers.

2.4. Optical characterization

Reflectance spectra of samples were acquired using a CRAIC micro-spectrophotometer 20/20 PV with 40 \times objective and approximately 20 $\mu\text{m} \times 20 \mu\text{m}$ aperture, to determine the spectral location of the plasmon resonance. The spectra were normalized by background subtraction of defective Au regions on PO to account for signals not associated with nanostructured bowtie regions. SERS measurements were conducted using a Renishaw Micro Raman system and a custom-built micro-Raman system with laser excitation wavelengths of 785 nm and 633 nm, respectively. Integration times were varied from 1 to 60 s, using a laser power of 5 mW for the 785 nm excitation and a power of approximately 600 μW for the 633 nm excitation. The illumination spot size was 2 μm in diameter for the 785 nm excitation, and the objective used for collection was 50 \times with a 0.75 NA. Measurements using 633 nm excitation had a spot size of approximately 1 μm and an objective of 60 \times and 0.8 NA was used. Samples were immersed in a 10⁻³ M solution of benzenethiol, serving as the analyte molecule, in deionized water for 18 h, followed by a methanol rinse to leave a molecular monolayer of benzenethiol on the Au bowtie regions. Neat benzenethiol Raman data were also collected for each laser to provide a standard for determining signal enhancement factors associated with the presence of Au bowtie arrays on the surface.

3. Results and discussion

3.1. Size tunability of bowties on transparent substrates

3.1.1. Sample fabrication. Au bowtie nanoantennas were formed by using NSL [20] on prestressed PO films. This fabrication process is depicted in figure 1. Prior to physical vapor deposition of Cr and Au, PS-COOH microspheres in the NSL mask were etched in 30 s oxygen plasma etch at a power of 20 W. The etching step increases the interstitial spacing between microspheres in the mask. Overall, this led to a more uniform nanotriangle size in the array. SEM images are presented in figure S1 in the supporting information stacks.iop.org/NANO/27/105302/mmedia, showing bowtie

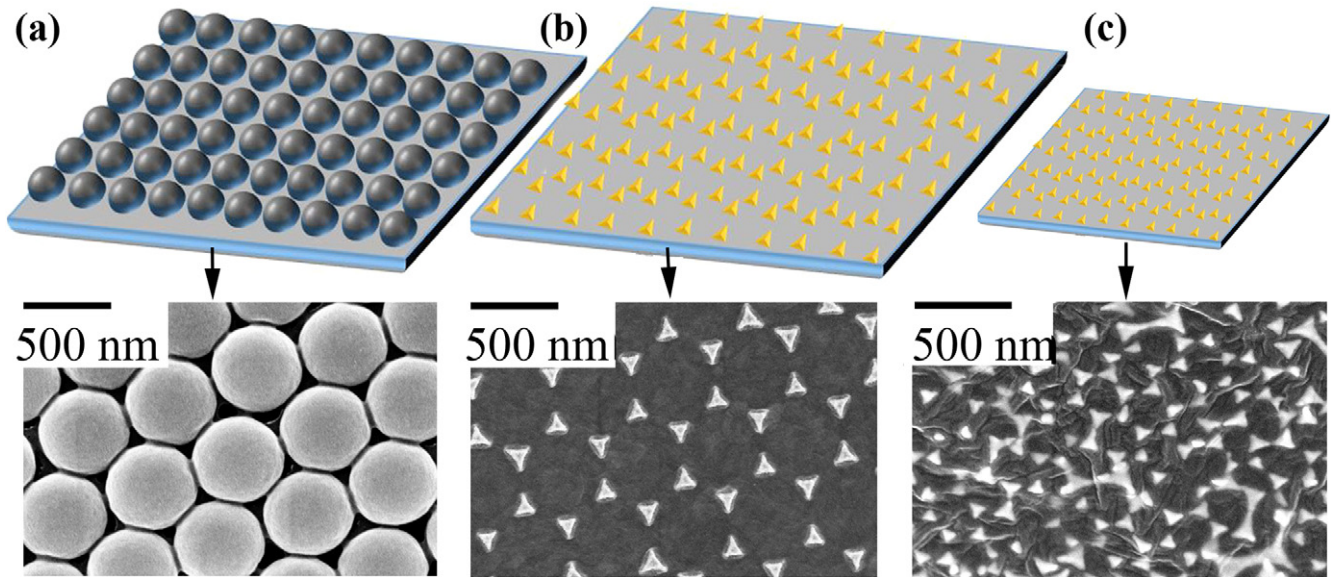


Figure 1. (Top row) Schematic of bowtie fabrication and (bottom row) SEM images of resulting structures. (a) A monolayer of hexagonal closed packed PS-COOH microspheres is spin coated on an oxygen plasma treated polyolefin (PO) film. (b) The substrate is then coated with 3 nm Cr followed by 40 nm of Au using physical vapor deposition, followed by sonication to release microspheres, to produce bowtie nanoantennas. (c) The substrates were mounted with double-sided tape onto a glass slide and placed in a convection oven to relieve prestress and reduce feature size. The SEM image corresponds to a sample processed at 135 °C.

nanoantenna arrays fabricated with and without etching the NSL mask. Plasma etching can induce oxidation of PO surfaces, leading to wrinkle formation as the prestress is relieved [50]. However, as the NSL mask covers most of the film, the PO film has minimal exposure during the process to introduce additional wrinkles. Any thin stiff layer on PO that is formed during the etching process would not add significant thickness to the Cr and Au layers deposited in the interstices of the microspheres. Therefore, we would not expect the process to affect the shrinkage or predicted wavelengths. Figure 1(b) shows a scanning electron microscopy (SEM) image of the resulting Au bowtie array created.

3.1.2. Bowtie nanoantenna structural transformation with prestress relief. The substrates were mounted on a polyester backing and then heated from room temperature (25 °C) to different temperatures ranging from 105 °C to 135 °C. The support of the flat polyester non-shrinking backing below the PO film prevents curling of the PO film and provides an additional standard to determine the size reduction. The macroscopic size reduction was measured with digital calipers in the two orthogonal directions in the sample plane (X:Y ratios) and is reported as a percent change in length in terms of the ratio of the final width relative to the initial width of the substrate. Processing temperatures of 105 °C, 115 °C and 135 °C led to a macroscopic size reduction in the length of the substrate by 38%, 52% and finally a maximum of 77%, respectively. These data are shown in the last column of table 1. The PO film exhibited non-uniformity in the X and Y directions at the lowest annealing temperature because the prestress is only partially relieved at these temperatures, and variations in the sample

Table 1. Summary of average measured size, standard deviation (SD) and size reduction of bowtie features as a function of processing temperature from SEM data. Reduction in the length of the PO film measured by digital calipers is shown in the last column.

| Processing temperature | Triangle height | Gap spacing (average % reduction) | Length reduction of PO film |
|------------------------|-----------------------------|-----------------------------------|-----------------------------|
| | and SD (average% reduction) | | |
| 25 °C | 90 ± 14 nm N/A | 85 ± 14 nm N/A | N/A |
| 105 °C | 85 ± 14 nm (6%) | 55 ± 17 nm (34%) | ΔX = 38% ΔY = 28% |
| 115 °C | 77 ± 16 nm (14%) | 37 ± 14 nm (56%) | ΔX = 52% ΔY = 52% |
| 135 °C | 60 ± 8 nm (33%) | 21 ± 10 nm (75%) | ΔX = 77% ΔY = 77% |

clamping may result in non-uniformity at partial stress relief [47].

SEM images were also obtained to examine the effect of processing temperatures on the nanoscale morphology of Au bowtie nanoantennas. In figure 2, SEM images reveal that as the PO films contract, the density of Au bowties increases while the average gap distance decreases. The average change in the measured gap spacing as a function of processing temperatures from the SEM images shown in figure 2 is summarized in table 1.

The SEM image of the non-heated sample at 25 °C, hereafter referred to as the reference sample, presented in figure 2(a), has a measured average gap distance of 85 ± 14 nm. At the final processing temperature of 135 °C, the gap distance was measured as 21 ± 10 nm in figure 2(d).

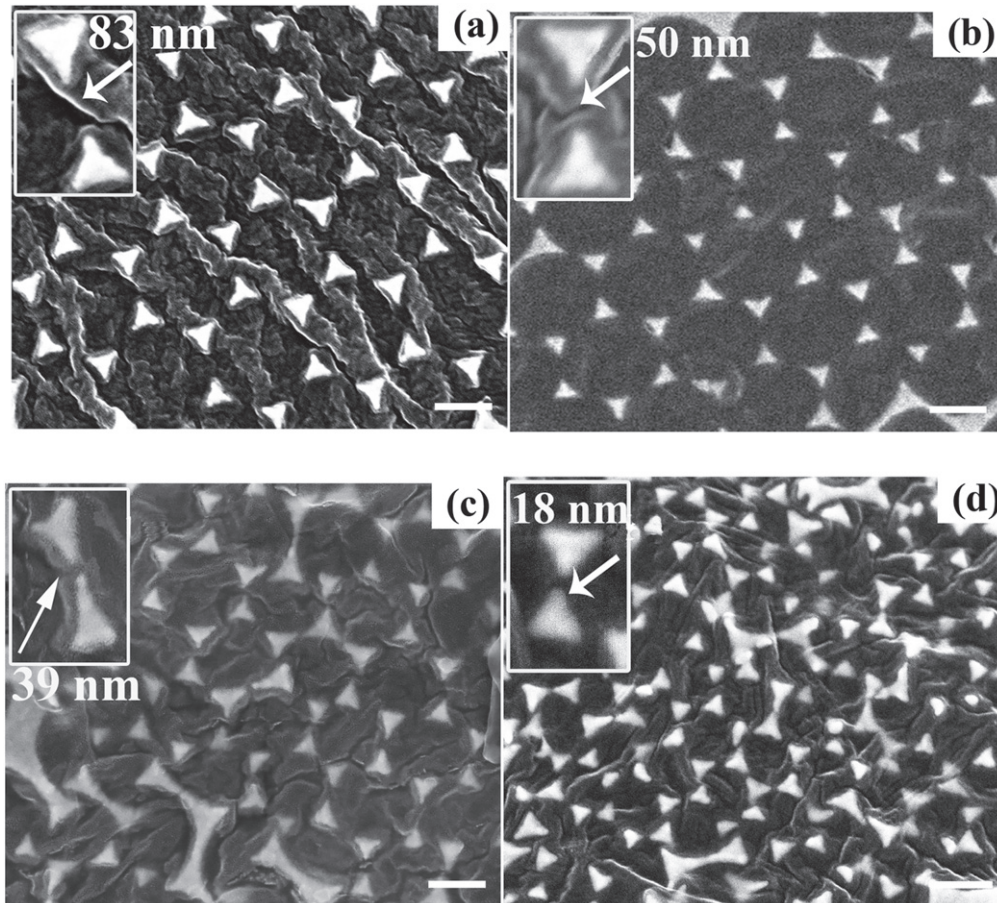


Figure 2. SEM images of Au bowtie nanoantennas on PO (a) as-deposited and heated at (b) 105 °C, (c) 115 °C, and (d) 135 °C. The scale bar is 200 nm. Insets show zoom levels in SEM images of a single bowtie nanoantenna to illustrate the average gap spacing.

Thus there is an average 75% reduction in the gap spacing with respect to the initial gap spacing when annealing between 105 °C to 135 °C. Overall, the changes measured in the gap spacing between individual bowtie triangles observed by SEM as a function of processing temperature is within standard deviation, consistent with those measured with digital calipers as reported in table 1. One means of evaluating the source of defects is to compare the standard deviations of the bowtie gaps as a function of processing temperature, summarized in table 1. The value of the standard deviation of the average gap spacing is not significantly different at the different processing temperatures. The standard deviation is 17 nm when processed at 105 °C and 14 nm for the reference sample. At the final process temperature, once the substrate has fully relieved the prestress, the standard deviation is 10 nm. The relatively small variation in standard deviation as a function of processing temperature indicates that the size reduction is reasonably uniform, in agreement with digital caliper measurements along the X and Y dimensions. SEM images were also analyzed to evaluate the defect density as a function of thermal processing temperature to evaluate whether defects are introduced during sample shrinking, as explained in the supporting information. SEM images are shown in figure S2. The defect density, as a function of processing temperature,

which has been summarized in table S1, is shown to remain basically constant. Thus it appears that the origin of defects is primarily related to the microsphere mask. While the size reduction does not lead to a considerable amount of new defects, the defect density will increase as the sample shrinks, as all features increase in density due to shrinking. This will lead to line broadening of the resonant wavelength observed in reflectance spectra.

When examining the data in table 1, it is significant to note that the average bowtie triangle height, defined as the distance between the tip and base center, has a smaller change than that of the gap spacing measured from the SEM images and the macroscopic decrease measured with digital calipers. Bowtie triangles on the reference sample have an average height of 90 nm. Processing temperatures of 105 °C and 115 °C do not lead to statistically significant changes, within standard deviation, in bowtie triangle height. Only at the maximum processing temperature, 135 °C, the height reduces to 60 nm, corresponding to an average 33% reduction in the height. This differs from the 77% macroscopic length reduction measured by digital calipers and the 75% reduction in gap spacing measured from the SEM images. This discrepancy can be explained in terms of the compressive stress that arises between Au bowtie nanoantennas and the PO substrate as the stress is released due to the higher elastic

modulus of Au (78 GPa) versus PO (0.45 MPa, provided by manufacturer). At lower processing temperatures, corresponding to a lower degree of prestress relief, the size reduction primarily occurs on the PO regions as the Au bowtie regions did not change significantly in size. At the maximum processing temperature, the smaller areal surface of triangles observed in SEM images, 33% height reduction is consistent with buckling of Au bowtie triangles. In previous work, Ross *et al* estimated the critical feature size and thickness for buckling of metal triangles with a constant biaxial contraction of 37.5%, assuming a uniform thin film with a circular delamination patch [43]. The height and metal thickness of bowtie triangles in figure 2 are in the buckling regime based on this analysis, yet it does not explain how buckling is affected by the magnitude of the prestress and finite feature sizes. It is understood that the characteristic buckling wavelength (λ_0) for a thin film on a thick substrate depends on the Young's modulus of Au (E_{Au}) and PO (E_{PO}), the Poisson ratio of Au (ν_{Au}) and PO (ν_{PO}), and the film thickness (t) [51, 52].

$$\lambda_0 = 2\pi t \left[\frac{E_{Au}(1 - \nu_{PO}^2)}{3(1 - \nu_{Au}^2)E_{PO}} \right]^{\frac{1}{3}} \quad (1)$$

Inserting values for E_{Au} (78 GPa), E_{PO} (0.45 MPa), ν_{Au} (0.44), ν_{PO} (0.49) and t (40 nm) yields a value of $9.5 \mu\text{m}$ for λ_0 . Yet recent non-linear analysis has shown that the characteristic wavelength will decrease when the film is in the large deformation limit, $>10\%$, and when features on the thermoplastic are smaller than λ_0 . In the large deformation limit the wavelength (λ) decreases according to [53]:

$$\lambda = \frac{\lambda_0}{(1 + \varepsilon_{Pre}) \left[1 + \frac{5\varepsilon_{Pre}(1 + \varepsilon_{Pre})}{32} \right]^{\frac{1}{3}}} = \lambda_0/1.88 \quad (2)$$

where ε_{Pre} is the amount of prestress in the substrate (77%); λ is also decreased due to the finite width (W) of the bowtie triangles that are smaller than λ_0 [54]:

$$\lambda = \lambda_0 \tanh \left\{ \frac{16}{15} \left(\frac{E_{PO}}{(1 - \nu_{PO}^2)} \frac{(1 - \nu_{Au}^2)}{E_{Au}} \right)^{\frac{1}{3}} \frac{W}{t} \right\}^{\frac{1}{4}} = 0.46 \lambda_0 \quad (3)$$

At full prestress relief, equations (2) and (3) will lead a value of λ of $2.3 \mu\text{m}$. This exceeds the feature size of bowtie triangles by approximately a factor of 20. Recently, Gao *et al* have determined that the critical strain for buckling, typically less than 1% for thin films [44], increases when feature size is much smaller than λ . In the case of Au nanodisk arrays on PDMS, finite element analysis predicts surface buckling will occur when the strain is as high as 44%, such that nanostructures approach one another [54]. Indeed, at the maximum processing temperature here, spacing between the bowtie nanotriangle gaps is observed to be less than 5 nm in some areas in SEM images. The statistically significant

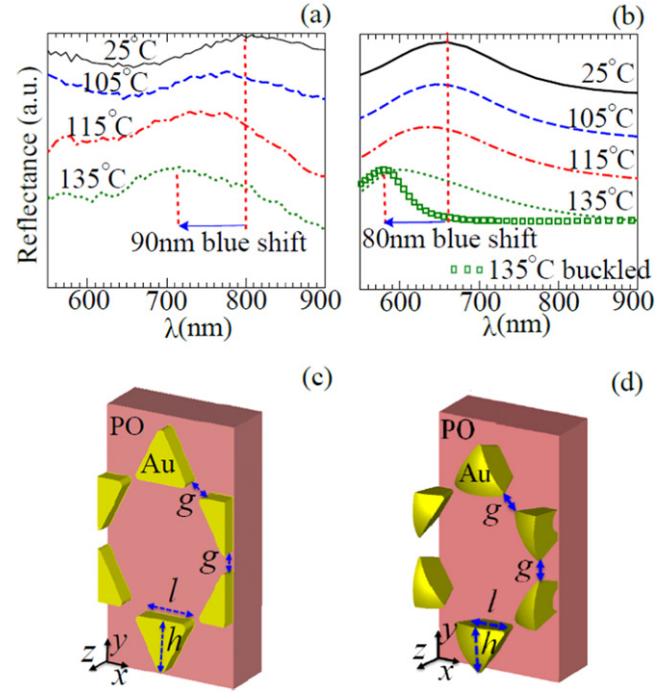


Figure 3. (a) Measured, and (b) simulated (without considering buckling deformations) reflectance spectra of the metasurface samples heated to different degrees of temperature under unpolarized incident wave illumination. For comparison purposes, the reflectance spectra of a metasurface sample heated to 135 °C is also simulated when including buckling deformation and plotted values (green hollow squares). The unit cell geometry of the periodic (c) unbuckled and (d) buckled bowtie arrays.

decrease in the observed bowtie triangle size and narrow local gap spacing in SEM images along with the analysis of the characteristic buckling λ are consistent with buckling only occurring at the maximum processing temperature.

3.2. Optical response of bowties on transparent substrates

3.2.1. Tunability of plasmon resonance. Prestressed PO provides an opportunity to design thermally tunable metasurfaces with additional control to produce non-planar structures. In this section, we show both numerically and experimentally how changing the processing temperature can control the reflectance spectra of bowtie nanoantenna arrays. Figure 3 shows measured and simulated reflectance spectra for the reference metasurface sample at 25 °C (solid black curve), and for samples heated to temperatures of 105 °C (dashed blue curve), 115 °C (dashed-dotted red curve) and 135 °C (green dotted curve). We observe from the measured results in figure 3(a) that the reference sample exhibits a plasmon resonance peak at approximately 800 nm, similar to the expected plasmon resonance of previously fabricated Au bowties of similar dimensions [43, 55]. As the processing temperature increases, the measured areal size of the bowtie triangles decreases (data tabulated in table 1), which causes a general trend of blue shift in the peak maxima of the measured reflectance, as shown in figure 3. It should be noted that as the processing temperature increases, the gap sizes

Table 2. Calculated SERS EFs of 998 cm^{-1} benzenethiol vibrational mode at both 785 nm and 633 nm excitations for bowtie arrays processed between $25\text{ }^{\circ}\text{C}$ – $135\text{ }^{\circ}\text{C}$.

| Processing temperature | Length reduction | Reflectance λ_{max} (nm) | EF 785 nm excitation | EF 633 nm excitation |
|-------------------------------|------------------|---|---------------------------|----------------------|
| $25\text{ }^{\circ}\text{C}$ | 0% | 800 | 2.2×10^6 | — |
| $105\text{ }^{\circ}\text{C}$ | 38% | 770 | $1.4\text{E} \times 10^7$ | 9.1×10^6 |
| $115\text{ }^{\circ}\text{C}$ | 52% | 730 | 1.2×10^6 | 8.3×10^7 |
| $135\text{ }^{\circ}\text{C}$ | 77% | 710 | 6.80×10^5 | — |

between bowtie triangles decrease, which in turn cause a red shift in the reflectance spectra. However, since the gap spacing is on average greater than 20 nm, bowtie triangles do not strongly interact with each other, causing an insignificant red shift. That is, the blue shift due to decreasing size dominates the reflectance spectra. The wavelength of the peak maxima in the measured reflectance data, λ_{max} , shifts from approximately 800 nm, to 770 nm, to 730 nm, to 710 nm when the processing temperature increases from room temperature, $25\text{ }^{\circ}\text{C}$, to $105\text{ }^{\circ}\text{C}$, $115\text{ }^{\circ}\text{C}$ and $135\text{ }^{\circ}\text{C}$, respectively, as summarized in table 2. There is a 90 nm blue shift in measured resonance wavelength between the reference sample and that heated to $135\text{ }^{\circ}\text{C}$, showing a wide range of tunability in the plasmon resonance wavelength using a PO surface.

The reflectance spectra of the bowtie nanoantenna array is also simulated in a fully periodic setup under normal incidence using the finite element method implemented in the CST Microwave Studio frequency domain solver. In order to understand how the reduction of feature size affects the optical response, we first neglect the buckling deformations in the simulations. Figure 3(c) shows the schematic of a unit cell of the periodic bowtie nanoantenna array without including buckling deformations. The unit cell dimensions for different processing temperatures are calculated using the average bowtie triangle dimensions provided in table 1. In the full-wave simulations we assume that: (i) as the processing temperature increases, the bowtie nanoantenna array remains periodic and the period and unit cell dimensions reduce as reported in table 1, (ii) the Au bowtie thickness (t) is invariant with heating temperature, and (iii) the heat treatment process does not affect the permittivity of the Au [56] and the PO substrate ($\epsilon_r = 3.2$). The simulated reflectance of the metasurface samples without considering the buckling deformations under unpolarized incident wave illumination is plotted in figure 3(b) for different processing temperatures. The reflectance for the unpolarized incident wave illumination is calculated by taking the arithmetic mean of the power reflectance for the x -polarized and y -polarized incident waves [57]. The broader linewidth observed in experimental reflectance data is partially attributed to the observed standard deviation in dimensions and gap spacing observed in bowtie arrays and increased defect density with sample shrinking. Aperiodic features result from defects in the NSL mask, most noticeably in figures 2(c) and (d). Common defects include misorientation in HCP domains, known as Fischer lines [58, 59], bowtie vacancies due to improper liftoff, and large-area Au deposition resulting from PS microsphere vacancies

[60–64]. Previous work has shown that optimizing the deposition method, including spin-coating parameters and surfactant concentration, can improve the uniformity of NSL masks [65–67], although that was not the focus of our work here. Electromagnetic simulations show a 65 nm blue shift in the resonant wavelength (from 660 nm to 595 nm) between the reference sample and the one heat-treated to $135\text{ }^{\circ}\text{C}$, when taking into account the decrease in nanotriangle size and gap spacing. The magnitude of this blue shift for this sample differs from the measured reflectance spectra shown in figure 3(a). Thus we also investigated how buckling deformations would affect the resonant wavelength and thereby reflectance spectra, which were not initially considered in the simulations. In order to model how triangular features evolve with prestress relief observed in SEM images, we use the straight-side buckling pattern, illustrated in figures 4(a)–(b), [68] to investigate the effect of bowtie triangles' buckling on the reflectance spectra. In this paper, we make the following assumptions: (i) the buckling deformation is smooth and of annular shape, (ii) the physical thickness, t , of the Au nanotriangle buckled over a distance l , shown in figure 4(b), is equal to the nanotriangle thickness in the unheated sample, shown in figure 4(a), (iii) the Au nanotriangle volume changes negligibly with the processing temperature, and (iv) the deformation on each side of the nanotriangle is symmetric with respect to its geometric axis.

The areal size of the bowtie nanoantennas has a smaller relative size reduction with respect to the reference sample than the gap spacing between nanotriangles for all samples. The unrestrained plastic (uncoated) regions shrink at these lower temperatures but the constrained (Au-coated) regions undergo less shrinkage. In order to determine the onset of thin film buckling, AFM topography images were acquired over $10\text{ }\mu\text{m} \times 10\text{ }\mu\text{m}$ regions and are shown in figure S3 in the supporting information. In both the reference sample and the sample annealed at $105\text{ }^{\circ}\text{C}$, an average height variation of approximately 45 nm is observed in line profiles taken across $10\text{ }\mu\text{m}$. This height variation corresponds well with the bowtie nanoantenna thickness. Thus, there is no evidence of thin film buckling on the sample annealed at $105\text{ }^{\circ}\text{C}$. The AFM topography image of figure S3 (c) for the sample processed at $115\text{ }^{\circ}\text{C}$ demonstrates that thin film buckling does result with prestress relief when the sample shrinks to 56% of its original length. Height variations on the order of 100 nm are observed that are consistent with expected amplitudes for thin film buckling [44]. However, we did not observe significant changes in plasmon resonance due to buckling in simulations since the nanotriangle size only changes by 14%. Thus, for

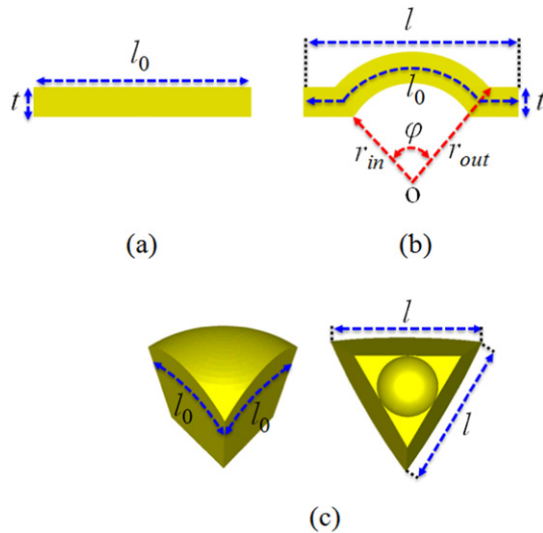


Figure 4. Schematic illustration of (a) an arbitrary unbuckled edge, and (b) its straight-side buckled equivalent. (c) 3D view of the buckled nanotriangle heated to 135 °C for which: $l = 52$ nm, $l_0 = 78$ nm, $r_{in} = 12.8$ nm, $r_{out} = 53$ nm, $\phi = 171.5^\circ$, $t = 40$ nm. In simulations we used l and l_0 for the length of nanotriangles' sides in the reference sample at 25 °C and the one heated to 135 °C, respectively, r_{in} and r_{out} are the inner and outer radii of the buckled surface, respectively, and ϕ represents the curvature.

the sake of simplicity, we only present how buckling deformations affect optical response for the sample processed at 135 °C, where buckling effects are observable in the morphology. Figure 4(c) shows the straight-side buckling model of an individual bowtie nanotriangle heated to 135 °C. The buckling model parameters for this sample are also provided in the caption of figure 4. Geometries chosen for simulations are consistent with those presented in [44] of nanostructures having a feature size well below λ_0 . The simulated reflectance spectra for the unbuckled (green dotted curve) and buckled samples (green hollow squares) at 135° processing temperature are plotted in figure 3(b). We observe that the reflectance spectra of the sample heated to 135° are blue shifted 15 nm more after considering the buckling deformations. The buckling deformations increase the thickness of the nanotriangles with respect to the polymer surface. Since the surrounding medium of the nanotriangle array is inhomogeneous, the electric fields between the nanotriangles spread in two media (air and polymer) having differing permittivity. Therefore, the term ‘effective permittivity’ is defined as the permittivity of an equivalent homogeneous medium surrounding the nanotriangle array such that it gives the same electromagnetic response as the nanotriangle array embedded in the inhomogeneous medium. The effective permittivity takes a value between the permittivities of the two media (air and polymer). As the thickness of nanotriangles increases, the fraction of the electric field that exists in the air medium increases, which in turn decreases the effective permittivity. The reduction in the effective permittivity of the array causes a blue shift in its reflectance spectra. An analogous blue shift is also observed in [69]. The overall simulated blue shift in the resonant wavelength between

the reference sample and the sample heated to 135 °C, considering the buckling deformations, is about 80 nm, which more closely agrees with the 90 nm measured blue shift observed in figure 3(a) than the shift for the sample not considering the buckling deformations. The difference between the simulated and the measured blue shifts in the reflectance spectra may also be partly attributed to thermal morphological changes in nanotriangles [70, 71]. Prior studies on nanorods have shown that even at temperatures as low as 100 °C, Au nanostructures can undergo thermal reshaping, particularly at higher aspect ratios, due to surface diffusion when annealed for 20 h [72]. Since the samples in this study were annealed for under an hour, any possible thermal reshaping would have occurred to a much lesser extent.

The electromagnetic simulations provide insight into the physical reasons behind the 90 nm measured blue shift due to prestress relief. However, the measured peaks of the reflectance spectra range from 710 nm to 800 nm but the simulated ones range from 580 nm to 660 nm. Some reasons for the difference between the measured and simulated reflectance peaks are that the optical properties of Au in the samples may be slightly different from those used in electromagnetic simulations [56], and even low-temperature annealing can change the morphology of high aspect ratio structures [70–72]. In addition, in the simulations, we assumed a fully periodic array of nanotriangles of uniform size having the measured average values tabulated in table 1. Defects and non-uniformity in the periodicity and size of nanotriangles in the measured samples, represented by a standard deviation in table 1, may also lead to a discrepancy between the measured and simulated reflectance spectra.

3.2.2. Surface-enhanced Raman scattering. Surfaces with Au bowtie nanoantennas were also characterized as SERS substrates. Au bowtie nanoantennas were immersed overnight in an aqueous solution of benzenethiol, which served as the analyte molecule. Following overnight incubation, the samples were rinsed in methanol to remove excess benzenethiol, leaving a molecular monolayer on the Au surfaces. SERS spectra of the benzenethiol-immersed samples acquired with laser excitation at 785 nm and 633 nm are shown in figures 5(a) and (b), respectively. For the 633 nm excitation, the laser power used was 600 μ W and the integration time used to was 60 s, as specified in the figure captions, while the laser power and integration time for the 785 nm excitation was 5 mW and 1 s for all samples. The position of the ν_1 , ν_2 , ν_3 and ν_4 known vibrational bands for benzenethiol are labeled in the figures for reference; they correspond to 998 ± 1 cm^{-1} , 1020 ± 2 cm^{-1} , 1070 ± 1 cm^{-1} and 1570 ± 2 cm^{-1} , respectively.

In figure 5(a), the intensity of the SERS benzenethiol peaks for the sample heated to 105 °C is approximately ten times higher when compared to the reference sample. According to the reflectance spectroscopy measurements, the LSPR wavelength of the sample heated to 105 °C is approximately 770 nm, while that of the reference sample is 800 nm. At higher processing temperatures, there is a blue shift of the LSPR wavelength. In figure 5(a), one can also

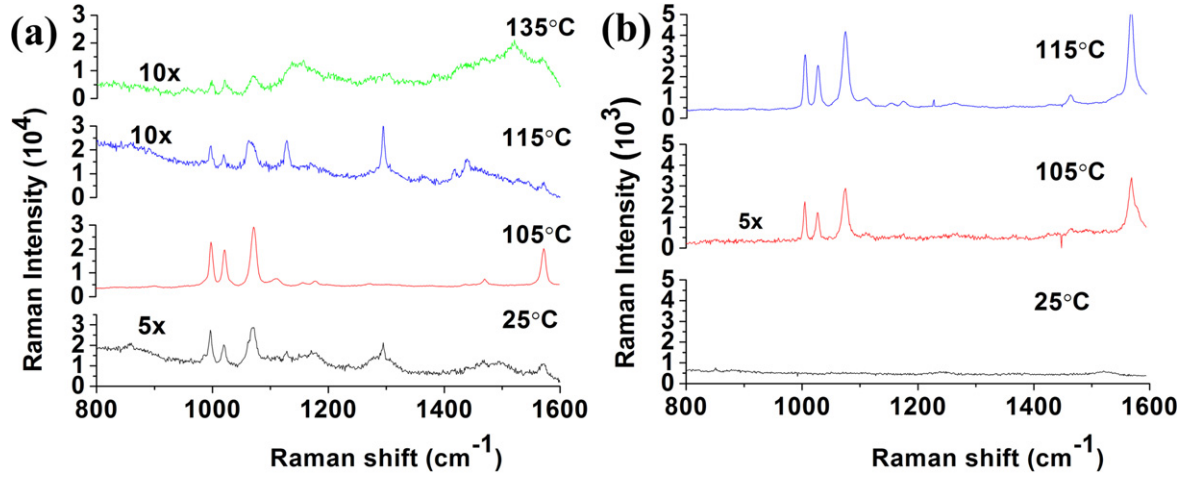


Figure 5. SERS spectra of a monolayer of benzenethiol on Au bowtie nanoantenna arrays processed at 105 °C (red curve), 115 °C (blue curve), 135 °C (green curve) and reference sample at 25 °C (black curve), using an excitation wavelength of (a) 785 nm and (b) 633 nm.

observe that the SERS intensity visibly decreases for the sample heated to 115 °C and there is a negligible SERS signal for the sample processed at 135 °C. As the stress is relieved at a higher processing temperature, the SERS intensity at 785 nm excitation decreases since the plasmon resonance blue shifts away from the excitation source. Thus, it is not unexpected that the sample processed at 105 °C would have a higher SERS enhancement than the other samples, since the plasmon resonance is close to the laser excitation wavelength. SERS data with an excitation wavelength of 633 nm are shown in figure 5(b). There is a negligible SERS signal observed for the reference sample in this case because the excitation wavelength is much lower than the LSPR wavelength. However, the samples processed at 105 °C and 115 °C both exhibit a measurable SERS signal when excited at 633 nm, even at integration times as low as 1 s. The SERS spectra of the samples heated to 115 °C relative to 105 °C have an approximate seven-fold increase in SERS signal intensity with 633 nm excitation. SERS spectra are not reported for the sample processed at 135 °C for the 633 nm excitation. This is due to the macroscopic roughness of this particular sample due to surface buckling, and the fact that the depth of focus of the objective in the experimental setup was not sufficient for adequate signal detection. In order to make quantitative comparisons, i.e., to normalize for different laser power and integration times, EFs were calculated for all the SERS data using the intensity of the 998 cm⁻¹ peak that corresponds to the C-H out of plane bending vibrational mode of benzenethiol. EFs are calculated according to equation (1) [73]:

$$EF = \frac{I_{\text{SERS}}/N_{\text{SERS}}}{I_{\text{neat}}/N_{\text{neat}}} \quad (4)$$

I_{SERS} and I_{neat} are the measured SERS and neat Raman intensities of the bowtie samples and neat solution, respectively. I_{SERS} is normalized with laser power, P , and

integration time, T , such that

$$I_{\text{SERS}} = \frac{I_{\text{neat}}}{P \times T} \quad (5)$$

The neat Raman intensity, I_{neat} , is normalized similarly. N_{SERS} and N_{neat} are the number of molecules in the measurement area of the fabricated samples and neat solution, respectively. N_{SERS} is found by normalizing the area in the laser spot size by the Au fractional coverage of the surface and the molecular surface coverage of benzenethiol on Au surfaces. The molecular surface coverage of a monolayer benzenethiol on the Au bowties is determined from the molar packing density on the Au surface, ρ_{surf} , which is reported to be 0.554 nmol cm⁻² [74], which is multiplied by Avogadro's number, N_{A} , to provide the molecular packing density. When this is multiplied by the laser spot size, A_{spot} , and the Au bowtie fractional coverage, f_{Au} , it provides the total number of molecules participating in the measurement, N_{SERS} ; that is

$$N_{\text{SERS}} = \rho_{\text{surf}} N_{\text{A}} \times f_{\text{Au}} A_{\text{spot}} \quad (6)$$

The fractional Au coverage relative to the laser spot size is calculated from SEM images. In order to determine the number of molecules measured in the neat solution, N_{neat} , one can multiply the concentration per unit volume of benzenethiol, 9.739 mmol cm⁻³, and V the scattering volume, where the latter is calculated by multiplying the spot size of the laser by the collection depth. It should be noted that in the case of the 633 nm enhancement factor calculation, a 5 μ l droplet of pure benzenethiol was dropcast to form a crystalline spot on a Au-covered slide, similar to methods [75–78]. When calculating the EF for 633 nm excitation, we must also take into account that the HeNe laser is polarized. Bowtie gaps have threefold symmetry and only when the laser polarization is aligned on the gap axis will there be significant excitation resulting in a large field enhancement. A waveplate was inserted during the measurement and indeed there were three major axes that had significant SERS

intensity. Thus, in the EF calculation the area was divided by a factor of three to take into account that only one-third of the structures contributed to the SERS intensity.

Table 2 lists the calculated EFs for Au bowtie nanoantennas as a function of processing temperature and laser excitation. Table 2 also lists the measured value of λ_{\max} from the reflectance spectra of each sample as this is associated with the LSPR wavelength of Au bowties. As shown in table 2, at 785 nm excitation wavelength, the EF has a maximum value of approximately 1.4×10^7 for the sample treated at 105 °C. While the plasmon resonance wavelength of the reference sample is near optimal at this excitation wavelength, as it is in between excitation and scattering light, when illuminated at 785 nm, the SERS EF for the sample processed at 105 °C is also almost an order of magnitude higher due to the smaller gap distances between the Au bowties, resulting in a stronger localized electric field in these regions and more confined plasmon fields [79, 80]. This demonstrates the importance of several design parameters to optimize SERS response in addition to LSPR frequency alone. At the 633 nm excitation, the samples processed at 105 °C and 115 °C showed EFs of 9.1×10^6 and 8.3×10^7 , respectively. The increase in EF correlates with the measured reflectance data, considering the plasmon resonance shifts from 770 nm to 710 nm when processing samples at 105 °C to 115 °C, thus moving toward the excitation wavelength. Overall, the increase in SERS EF shows the flexibility of the PO film and the ability to tune the plasmon resonance of the bowtie array through a quick, robust heating process. This described fabrication method is thus a way to engineer a SERS response at a desired wavelength. Overall, the data in table 2 reveal that the maximum SERS signal is measured when both the excitation and Raman scattered light are near the plasmon resonance wavelength, and the ability to tune the resonance is achieved using the PO film.

4. Conclusion

We demonstrate that the size and morphology of Au bowtie nanoantenna arrays, fabricated using an NSL mask on PO thermoplastic films, is controllable by varying the processing temperature, post-nanopattern formation. Accordingly, the optical properties of the bowtie nanoantenna array, such as LSPR wavelength and SERS enhancement, are also tunable. Furthermore, the average gap spacing can be reduced up to 75% when the processing temperature increases from 25 °C to 135 °C. Changes in bowtie size, gap spacing and buckling lead to a blue shift in the plasmon resonance wavelength with a tunable window of around 90 nm, which is observed in both reflectance spectroscopy measurements and full-wave simulations. SERS spectra were measured and correlated with the measured LSPR wavelength. The highest calculated EF was 8.3×10^7 . Tunability of the plasmon resonances with simple processing conditions allowed for this EF to be measurable for both the 785 nm and 633 nm excitations.

Using smaller PS spheres in the NSL mask would reduce the initial gap spacing and lead to a higher EF. It is well

known that the gap spacing between bowtie nanoantennas approaching the single nanometer distances leads to extremely high localized electric fields that are useful for achieving hot spots for SERS [33–35]. Moreover, this work suggests the possibility of integrating PO films with higher resolution fabrication techniques, such as electron beam lithography, to create highly organized and controllably spaced patterns with nanometer resolutions.

Acknowledgments

The authors acknowledge the National Science Foundation EECs- 1449397, CMMI- 1360060 and NIH 1DP2OD007283 for funding this work. The authors also acknowledge the use of the facilities within the Laser Spectroscopy Facility and the Laboratory for Electron and X-ray Instrumentation (LEXI) center at the University of California, Irvine. The authors would like to thank the Chemistry Department, including Dr Jeffrey C Owrutsky and Dr Stanislav D Tsoi, at the Naval Research Laboratories in Washington D C, for the use of their CRAIC micro-spectrophotometer for the reflectance measurements. The authors would also like to thank Dr Wickramasinghe for allowing them to set up an optical system for Raman measurements acquired at 633 nm excitation in his laboratory. The authors would also like to thank Computer Simulation Technology (CST) for providing the CST Microwave Studio software for electromagnetic simulations, which was instrumental for this investigation. The authors would also like to acknowledge Bakr Teebi for his help in the fabrication of polystyrene nanosphere lithography masks.

References

- [1] Fleischmann M, Hendra P J and McQuillan A J 1974 Raman spectra of pyridine adsorbed at a silver electrode *Chem. Phys. Lett.* **26** 163–6
- [2] Nie S and Emory S R 1997 Probing single molecules and single nanoparticles by surface-enhanced raman scattering *Science* **275** 1102–6
- [3] Kneipp K, Wang Y, Kneipp H, Perelman L T, Itzkan I, Dasari R R and Feld M S 1997 Single molecule detection using surface-enhanced raman scattering (SERS) *Phys. Rev. Lett.* **78** 1667–70
- [4] Jensen T R, Malinsky M D, Haynes C L and Van Duyne R P 2000 Nanosphere lithography: tunable localized surface plasmon resonance spectra of silver nanoparticles *J. Phys. Chem. B* **104** 10549–56
- [5] Deng W, Xie F, Baltar H T M C M and Goldys E M 2013 Metal-enhanced fluorescence in the life sciences: here, now and beyond *Phys. Chem. Chem. Phys.* **15** 15695–708
- [6] Sharma H, Digman M A, Felsing N, Gratton E and Khine M 2014 Enhanced emission of fluorophores on shrink-induced wrinkled composite structures *Opt. Mater. Express* **4** 753–63
- [7] Westphalen M, Kreibitz U, Rostalski J, Lüth H and Meissner D 2000 Metal cluster enhanced organic solar cells *Sol. Energy Mater. Sol. Cells* **61** 97–105
- [8] Feng A L, You M L, Tian L, Singamaneni S, Liu M, Duan Z, Lu T J, Xu F and Lin M 2015 Distance-dependent plasmon-enhanced fluorescence of upconversion nanoparticles using

- polyelectrolyte multilayers as tunable spacers *Sci. Rep.* **5** 7779
- [9] Hylton N P et al 2013 Loss mitigation in plasmonic solar cells: aluminium nanoparticles for broadband photocurrent enhancements in GaAs photodiodes *Sci. Rep.* **3** 2874
- [10] Akimov Y A and Koh W S 2010 Resonant and nonresonant plasmonic nanoparticle enhancement for thin-film silicon solar cells *Nanotechnology* **21** 235201
- [11] Kelly K L, Coronado E, Zhao L L and Schatz G C 2003 The optical properties of metal nanoparticles: the influence of size, shape, and dielectric environment *J. Phys. Chem. B* **107** 668–77
- [12] Campione S, Guclu C, Ragan R and Capolino F 2013 Fano resonances in metasurfaces made of linear trimers of plasmonic nanoparticles, *Opt. Lett.* **38** 5216–9
- [13] Campione S, de Ceglia D, Guclu C, Vincenti M A, Scalora M and Capolino F 2014 Fano collective resonance as complex mode in a two-dimensional planar metasurface of plasmonic nanoparticles *Appl. Phys. Lett.* **105** 191107
- [14] Campione S, Guclu C, Ragan R and Capolino F 2014 Enhanced magnetic and electric fields via fano resonances in metasurfaces of circular clusters of plasmonic nanoparticles *ACS Photonics* **1** 254–60
- [15] Manfrinato V R, Zhang L, Su D, Duan H, Hobbs R G, Stach E A and Berggren K K 2013 Resolution limits of electron-beam lithography toward the atomic scale *Nano Lett.* **13** 1555–8
- [16] Vieu C, Carcenac F, Pépin A, Chen Y, Mejjias M, Lebib A, Manin-Ferlazzo L, Couraud L and Launois H 2000 Electron beam lithography: resolution limits and applications *Appl. Surf. Sci.* **164** 111–7
- [17] Roxworthy B J, Bhuiya A M, Yu X, Chow E K C and Toussaint K C Jr 2014 Reconfigurable nanoantennas using electron-beam manipulation *Nat. Commun.* **5** 4427
- [18] Melngailis J 1993 Focused ion beam lithography *Nucl. Instrum. Methods Phys. Res. B* **80–81** 1271–80
- [19] Acikgoz C, Hempenius M A, Huskens J and Vancso G J 2011 Polymers in conventional and alternative lithography for the fabrication of nanostructures *Eur. Polym. J.* **47** 2033–52
- [20] Hulteen J C and Duyne R P V 1995 Nanosphere lithography: a materials general fabrication process for periodic particle array surfaces *J. Vac. Sci. Technol. A* **13** 1553–8
- [21] Choi J H, Adams S M and Ragan R 2009 Design of a versatile chemical assembly method for patterning colloidal nanoparticles *Nanotechnology* **20** 065301
- [22] Adams S M, Campione S, Capolino F and Ragan R 2013 Directing cluster formation of au nanoparticles from colloidal solution *Langmuir* **29** 4242–51
- [23] Lee M H, Huntington M D, Zhou W, Yang J-C and Odom T W 2011 Programmable soft lithography: solvent-assisted nanoscale embossing *Nano Lett.* **11** 311–5
- [24] Abécassis B, Tessier M D, Davidson P and Dubertret B 2014 Self-assembly of CdSe nanoplatelets into giant micrometer-scale needles emitting polarized light *Nano Lett.* **14** 710–5
- [25] Diroll B T, Greybush N J, Kagan C R and Murray C B 2015 Smectic nanorod superlattices assembled on liquid subphases: structure, orientation, defects, and optical polarization *Chem. Mater.* **27** 2998–3008
- [26] Thorkelsson K, Nelson J H, Alivisatos A P and Xu T 2013 End-to-End alignment of nanorods in thin films *Nano Lett.* **13** 4908–13
- [27] Chang J-B, Choi H K, Hannon A F, Alexander-Katz A, Ross C A and Berggren K K 2014 Design rules for self-assembled block copolymer patterns using tiled templates *Nat. Commun.* **5** 3305
- [28] Pryce I M, Kelaita Y A, Aydin K and Atwater H A 2011 Compliant metamaterials for resonantly enhanced infrared absorption spectroscopy and refractive index sensing *ACS Nano* **5** 8167–74
- [29] Pryce I M, Aydin K, Kelaita Y A, Briggs R M and Atwater H A 2010 Highly strained compliant optical metamaterials with large frequency tunability *Nano Lett.* **10** 4222–7
- [30] Aksu S, Huang M, Artar A, Yanik A A, Selvarasah S, Dokmeci M R and Altug H 2011 Flexible plasmonics on unconventional and nonplanar substrates *Adv. Mater.* **23** 4422–30
- [31] Sharac N, Sharma H, Khine M and Ragan R Tunable nano bead arrays on film for controlling propagation of light *Proc. SPIE* **8809** 88091O
- [32] Nguyen D, Taylor D, Qian K, Norouzi N, Rasmussen J, Botzet S, Lehmann M, Halverson K and Khine M 2010 Better shrinkage than Shrinky-Dinks *Lab Chip* **10** 1623–6
- [33] Jäckel F, Kinkhabwala A A and Moerner W E 2007 Gold bowtie nanoantennas for surface-enhanced Raman scattering under controlled electrochemical potential *Chem. Phys. Lett.* **446** 339–343
- [34] Hatab N A, Hsueh C-H, Gaddis A L, Retterer S T, Li J-H, Eres G, Zhang Z and Gu B 2010 Free-standing optical gold bowtie nanoantenna with variable gap size for enhanced Raman spectroscopy *Nano Lett.* **10** 4952–5
- [35] Dodson S, Haggui M, Bachelot R, Plain J, Li S and Xiong Q 2013 Optimizing electromagnetic hotspots in plasmonic bowtie nanoantennae *J. Phys. Chem. Lett.* **4** 496–501
- [36] Schuck P J, Fromm D P, Sundaramurthy A, Kino G S and Moerner W E 2005 Improving the mismatch between light and nanoscale objects with gold bowtie nanoantennas *Phys. Rev. Lett.* **94** 017402
- [37] Kinkhabwala A A 2010 Coupling Fluorophores Molecules to Nanophotonic Structures *PhD Thesis* Stanford University
- [38] Hatab N A, Hsueh C-H, Gaddis A L, Retterer S T, Li J-H, Eres G, Zhang Z and Gu B 2010 Free-standing optical gold bowtie nanoantenna with variable gap size for enhanced Raman spectroscopy *Nano Lett.* **10** 4952–5
- [39] Dodson S, Haggui M, Bachelot R, Plain J, Li S and Xiong Q 2013 Optimizing electromagnetic hotspots in plasmonic bowtie nanoantennae *J. Phys. Chem. Lett.* **4** 496–501
- [40] Bowden N, Brittain S, Evans A G, Hutchinson J W and Whitesides G M 1998 Spontaneous formation of ordered structures in thin films of metals supported on an elastomeric polymer *Nature* **393** 146–9
- [41] Huck W T S, Bowden N, Onck P, Pardoën T, Hutchinson J W and Whitesides G M 2000 Ordering of spontaneously formed buckles on planar surfaces *Langmuir* **16** 3497–501
- [42] Xiao J, Jiang H, Khang D-Y, Wu J, Huang Y and Rogers J A 2008 Mechanics of buckled carbon nanotubes on elastomeric substrates *J. Appl. Phys.* **104** 033543
- [43] Ross B M, Wu L Y and Lee L P 2011 Omnidirectional 3D nanoplasmonic optical antenna array via soft-matter transformation *Nano Lett.* **11** 2590–5
- [44] Gao L et al 2015 Optics and nonlinear buckling mechanics in large-area, highly stretchable arrays of plasmonic nanostructures *ACS Nano* **9** 5968–75
- [45] Cooper C T, Rodriguez M, Blair S and Shumaker-Parry J S 2014 Polarization anisotropy of multiple localized plasmon resonance modes in noble metal nanocrescents *J. Phys. Chem. C* **118** 1167–73
- [46] Chen K, Rajeeva B B, Wu Z, Rukavina M, Dao T D, Ishii S, Aono M, Nagao T and Zheng Y 2015 'Moiré Nanosphere Lithography,' *ACS Nano* **9** 6031–40
- [47] Dyer D, Shreim S, Jayadev S, Lew V, Botvinick E and Khine M 2011 Sequential shrink photolithography for plastic microlens arrays *Appl. Phys. Lett.* **99** 034102
- [48] Scheeler S P, Mühlig S, Rockstuhl C, Hasan S B, Ullrich S, Neubrech F, Kuderer S and Pacholski C 2013 Plasmon coupling in self-assembled gold nanoparticle-based honeycomb islands *J. Phys. Chem. C* **117** 18634–41

- [49] Cha H, Yoon J H and Yoon S 2014 Probing quantum plasmon coupling using gold nanoparticle dimers with tunable interparticle distances down to the subnanometer range *ACS Nano* **8** 8554–63
- [50] Chen A et al 2011 Shrink-film configurable multiscale wrinkles for functional alignment of human embryonic stem cells and their cardiac derivatives *Adv. Mater.* **23** 5785–91
- [51] Chen X and Hutchinson J W 2004 Herringbone buckling patterns of compressed thin films on compliant substrates *J. Appl. Mech.* **71** 597–603
- [52] Huang Z Y, Hong W and Suo Z 2005 Nonlinear analyses of wrinkles in a film bonded to a compliant substrate *J. Mech. Phys. Solids* **53** 2101–18
- [53] Jiang H, Khang D-Y, Song J, Sun Y, Huang Y and Rogers J A 2007 Finite deformation mechanics in buckled thin films on compliant supports *Proc. Natl. Acad. Sci.* **104** 15607–12
- [54] Jiang H, Khang D-Y, Fei H, Kim H, Huang Y, Xiao J and Rogers J A 2008 Finite width effect of thin-films buckling on compliant substrate: experimental and theoretical studies *J. Mech. Phys. Solids* **56** 2585–98
- [55] Zheng P, Cushing S K, Suri S and Wu N 2015 Tailoring plasmonic properties of gold nanohole arrays for surface-enhanced Raman scattering *Phys. Chem. Chem. Phys.* **17** 21211–9
- [56] Johnson P B and Christy R W 1972 Optical constants of the noble metals *Phys. Rev. B* **6** 4370–9
- [57] Born M and Wolf E 1959 *Principles of Optics: Electromagnetic Theory of Propagation, Interference, and Diffraction of Light* (London: Pergamon)
- [58] Fischer U C and Zingsheim H P 1981 Submicroscopic pattern replication with visible light *J. Vac. Sci. Technol.* **19** 881–5
- [59] Gonçalves M R, Siegel A and Marti O 2008 Influence of the light-scattering form factor on the Bragg diffraction patterns of arrays of metallic nanoparticles *J. Microsc.* **229** 475–82
- [60] Zhang Q, Tan Y, Xie J and Lee J 2009 Colloidal synthesis of plasmonic metallic nanoparticles *Plasmonics* **4** 9–22
- [61] Colson P, Henrist C and Cloots R 2013 Nanosphere lithography: a powerful method for the controlled manufacturing of nanomaterials *J. Nanomater.* 984510
- [62] Haynes C L and Van Duyne R P 2001 Nanosphere lithography: a versatile nanofabrication tool for studies of size-dependent nanoparticle optics *J. Phys. Chem. B* **105** 5599–611
- [63] Ormonde A D, Hicks E C M, Castillo J and Van Duyne R P 2004 Nanosphere lithography: fabrication of large-area ag nanoparticle arrays by convective self-assembly and their characterization by scanning uv-visible extinction spectroscopy *Langmuir* **20** 6927–31
- [64] Canpean V and Astilean S 2009 Extending nanosphere lithography for the fabrication of periodic arrays of subwavelength metallic nanoholes *Mater. Lett.* **63** 2520–2
- [65] Jiang P and McFarland M J 2004 Large-scale fabrication of wafer-size colloidal crystals, macroporous polymers and nanocomposites by spin-coating *J. Am. Chem. Soc.* **126** 13778–86
- [66] Stavroulakis P I, Christou N and Bagnall D 2009 Improved deposition of large scale ordered nanosphere monolayers via liquid surface self-assembly *Mater. Sci. Eng. B* **165** 186–9
- [67] Liu X, Gozubenli N, Choi B, Jiang P, Meagher T and Jiang B 2015 Templated fabrication of periodic arrays of metallic and silicon nanorings with complex nanostructures *Nanotechnology* **26** 055603
- [68] Wang S and Li Z 2011 Mathematical modeling and numerical simulation of telephone cord buckles of elastic films *Sci. China Math.* **54** 1063–76
- [69] Lin T-R, Chang S-W, Chuang S L, Zhang Z and Schuck P J 2010 Coating effect on optical resonance of plasmonic nanobowtie antenna *Appl. Phys. Lett.* **97** 063106
- [70] Roxworthy B J, Bhuiya A M, Inavalli V V G K, Chen H and Toussaint K C 2014 Multifunctional plasmonic film for recording near-field optical intensity *Nano Lett.* **14** 4687–93
- [71] Taylor A B, Siddiquee A M and Chon J W M 2014 Below melting point photothermal reshaping of single gold nanorods driven by surface diffusion *ACS Nano* **8** 12071–9
- [72] Petrova H, Juste J P, Pastoriza-Santos I, Hartland G V, Liz-Marzán L M and Mulvaney P 2006 On the temperature stability of gold nanorods: comparison between thermal and ultrafast laser-induced heating *Phys. Chem. Chem. Phys.* **8** 814–21
- [73] Camargo P H C, Cobley C M, Rycenga M and Xia Y 2009 Measuring the surface-enhanced Raman scattering enhancement factors of hot spots formed between an individual Ag nanowire and a single Ag nanocube *Nanotechnology* **20** 434020
- [74] Gui J Y, Stern D A, Frank D G, Lu F, Zapfen D C and Hubbard A T 1991 Adsorption and surface structural chemistry of thiophenol, benzyl mercaptan, and alkyl mercaptans. Comparative studies at silver(111) and platinum (111) electrodes by means of Auger spectroscopy, electron energy loss spectroscopy, low energy electron diffraction and electrochemistry *Langmuir* **7** 955–63
- [75] Das G, Patra N, Gopalakrishnan A, Zaccaria R P, Toma A, Thorat S, Di Fabrizio E, Diaspro A and Salerno M 2012 Fabrication of large-area ordered and reproducible nanostructures for SERS biosensor application *Analyst* **137** 1785–92
- [76] Xu Z, Wu H-Y, Ali S U, Jiang J, Cunningham B T and Liu G L 2011 Nanoreplicated positive and inverted submicrometer polymer pyramid array for surface-enhanced Raman spectroscopy *J. Nanophotonics* **5** 053526
- [77] Jackson J B and Halas N J 2004 Surface-enhanced Raman scattering on tunable plasmonic nanoparticle substrates *Proc. Natl Acad. Sci. USA* **101** 17930–5
- [78] Yan B, Thubagere A, Premasiri W R, Ziegler L D, Dal Negro L and Reinhard B M 2009 Engineered SERS Substrates with multiscale signal enhancement: nanoparticle cluster arrays *ACS Nano* **3** 1190–202
- [79] Fischer H and Martin O J F 2008 Engineering the optical response of plasmonic nanoantennas *Opt. Express* **16** 9144–54
- [80] Yan Z, Chen X, Du W, Chen Z, Zhan P, Wang H-T and Wang Z 2014 Near-field plasmonic coupling for enhanced nonlinear absorption by femtosecond pulses in bowtie nanoantenna arrays *Appl. Phys.* **117** 1841–8